

Article

# Four-Polarisation Camera for Anisotropy Mapping at Three Orientations: Micro-Grain of Olivine

Shuji Kamegaki <sup>1,†</sup> , Daniel Smith <sup>2,†</sup> , Meguya Ryu <sup>3</sup> , Soon Hock Ng <sup>2</sup> , Hsin-Hui Huang <sup>2</sup> , Pegah Maasoumi <sup>2</sup>, Jitraporn Vongsvivut <sup>4</sup> , Daniel Moraru <sup>5</sup> , Tomas Katkus <sup>2</sup>, Saulius Juodkazis <sup>2,6,\*</sup>  and Junko Morikawa <sup>1,6,\*</sup>

- <sup>1</sup> CREST-JST and School of Materials and Chemical Technology, Tokyo Institute of Technology, Ookayama, Meguro-ku, Tokyo 152-8550, Japan; kamegaki.s.aa@m.titech.ac.jp
- <sup>2</sup> Optical Sciences Centre, ARC Training Centre in Surface Engineering for Advanced Materials (SEAM), School of Science, Swinburne University of Technology, Hawthorn, VIC 3122, Australia; danielsmith@swin.edu.au (D.S.); soonhockng@swin.edu.au (S.H.N.); hsinhuihuang@swin.edu.au (H.-H.H.); pmaasoumi@swin.edu.au (P.M.); tkatkus@swin.edu.au (T.K.)
- <sup>3</sup> National Metrology Institute of Japan (NMIJ), National Institute of Advanced Industrial Science and Technology (AIST), Tsukuba Central 3, 1-1-1 Umezono, Tsukuba 305-8563, Japan; ryu.meguya@aist.go.jp
- <sup>4</sup> ANSTO-Australian Synchrotron, Infrared Microspectroscopy (IRM) Beamline, 800 Blackburn Road, Clayton, VIC 3168, Australia; jitrapov@ansto.gov.au
- <sup>5</sup> Research Institute of Electronics, Shizuoka University, Johoku 3-5-1, Hamamatsu 432-8011, Japan; moraru.daniel@shizuoka.ac.jp
- <sup>6</sup> WRH Program International Research Frontiers Initiative (IRFI) Tokyo Institute of Technology, Nagatsuta-cho, Midori-ku, Yokohama 226-8503, Japan
- \* Correspondence: sjuodkazis@swin.edu.au (S.J.); morikawa.j.aa@m.titech.ac.jp (J.M.)
- † These authors contributed equally to this work.

**Abstract:** A four-polarisation camera was used to map the absorbance of olivine micro-grains before and after high-temperature annealing (HTA). It is shown that HTA of olivine xenoliths at above 1200 °C in O<sub>2</sub> flow makes them magnetised. Different modes of operation of the polariscope with polarisation control before and after the sample in transmission and reflection modes were used. The reflection type was assembled for non-transparent samples of olivine after HTA. The sample for optical observation in transmission was placed on an achromatic, plastic, quarter-wavelength waveplate as a sample holder. Inspection of the sample's birefringence (retardance), as well as absorbance, was undertaken. The best fit for the transmitted intensity or transmittance  $T$  (hence, absorbance  $A = -\log_{10} T$ ) is obtainable using a simple best fit with only three orientations (from the four orientations measured by the camera). When the intensity of transmitted light at one of the orientations is very low due to a cross-polarised condition (polariser–analyser arrangement), the three-point fit can be used. The three-point fit in transmission and reflection modes was validated for  $T(\theta) = Amp \times \cos(2\theta - 2\theta_{shift}) + offset$ , where the amplitude  $Amp$ , offset  $offset$ , and orientation azimuth  $\theta_{shift}$  were extracted for each pixel via the best fit.

**Keywords:** anisotropy; polarisation analysis; Stokes parameters; polarimetry; olivine



**Citation:** Kamegaki, S.; Smith, D.; Ryu, M.; Ng, S.H.; Huang, H.-H.; Maasoumi, P.; Vongsvivut, J.; Moraru, D.; Katkus, T.; Juodkazis, S.; et al. Four-Polarisation Camera for Anisotropy Mapping at Three Orientations: Micro-Grain of Olivine. *Coatings* **2023**, *13*, 1640. <https://doi.org/10.3390/coatings13091640>

Academic Editor: Alexandre Botas

Received: 12 August 2023

Revised: 10 September 2023

Accepted: 11 September 2023

Published: 18 September 2023



**Copyright:** © 2023 by the authors. Licensee MDPI, Basel, Switzerland. This article is an open access article distributed under the terms and conditions of the Creative Commons Attribution (CC BY) license (<https://creativecommons.org/licenses/by/4.0/>).

## 1. Introduction

Colour is one of the most popular qualitative inspection tools in the microscopic observation of minerals. Cross-polarised imaging together with full-wave  $\lambda = 530$  nm or quarter-waveplate  $\lambda/4 = 147.3$  nm inserted at a  $\pi/4$  orientation to the cross-Nikol setup can be utilised to obtain vivid colours that represent optical retardance. For example, the 530 nm wavelength will be blocked in a cross-Nikol setup with such a waveplate, while the other RGB colours will undergo different degrees of retardance, causing a magenta-coloured background (no sample). Colour can indicate the presence of  $\Delta n \times d$  (i.e., birefringence  $\Delta n$ ) and the total difference in optical thickness due to physical thickness  $d$  at a

location on the sample. More information can be extracted using images taken with different linear polarisations; e.g., the absorbance  $A = -\log_{10} T$  from the measured transmittance  $T = I_T/I_0$  can be determined. Here,  $I_{T,0}$  are the transmitted and incident intensities, respectively. However, due to the unevenness of natural samples, imaging at different sample (or polariser) orientations brings about lateral shifts, as well as distortions, in the image. This limits the application potential of imaging at different polarisations when either the sample or polariser has to be rotated between image acquisitions.

The motivation for this study was to use polarisation-resolved imaging at visible wavelengths  $\lambda \sim 0.5 \mu\text{m}$  and comparable resolution  $(1-2) \times \lambda$  for mapping the complex morphologies of naturally occurring micro-crystals, which is typical in research on mineral resource exploration, volcanic lava flows or fallout particles from eruptions, meteorites, etc. Usually, such 0.1–1 mm grains are analysed at IR wavelengths in the chemical fingerprinting spectral range of  $\lambda \sim (12-2) \mu\text{m}$  (in wavenumbers,  $\tilde{\nu} = (833-5000) \text{cm}^{-1}$ ), where the spatial resolution is markedly reduced  $\propto \lambda$  [1,2]. Moreover, the crystalline and glass absorption under specific phonon modes defining micro-volumes of specific materials/crystals is studied even at the longer wavelengths in the THz domain with wavenumbers  $20-700 \text{cm}^{-1}$  or  $\lambda = (500-14) \mu\text{m}$  at a further reduced spatial resolution [2]. Here, we used high-optical-resolution imaging with a resolution of  $\sim 1 \mu\text{m}$  to identify structure and morphology changes due to inhomogeneous composition, grain, boundaries, mass density swirls, etc., which have paramount importance in the formation of new phases and materials during annealing. Optical images with high quality and resolution that reveal anisotropy in absorbance, retardance, or reflectance can be correlated with IR–THz maps (chemical, phonon) with low spatial resolution and combined/correlated with Raman and Brillouin imaging of (visco)mechanical/elastic properties at the micro-scale [3,4]. We have demonstrated that anisotropies in absorption and/or retardance can be detected via orientation azimuth angles even when the spatial resolution is more than 10 times lower [5,6]. This makes comparison of anisotropy mapping at resolutions that differ by 100 times a potentially useful tool for correlations throughout the visible–IR–THz spectra (1–10–100  $\mu\text{m}$ ). As a prototype sample, we used a volcanic olivine xenolith ( $\text{Fe, Mg}_2\text{SiO}_4$ ) (Mortlake, Australia). Olivine is an orthorhombic,  $Pbnm$ -space-group, birefringent mineral and, as the major constituent of the Earth's mantle, contributes Fe to its core, defining the Earth's magnetic properties. We show here that olivine in xenoliths becomes magnetized after high-temperature annealing (HTA) above  $1300 \text{ }^\circ\text{C}$  in  $\text{O}_2$  flow. Current hypotheses suggest that Mg-rich olivine (forsterite) has precipitations of magnetite  $\text{Fe}_3\text{O}_4$  ( $\text{Fe}^{2+}\text{Fe}_2^{3+}\text{O}_4$ ) along the defects and crystallite boundaries, similar to those observed in volcanic olivines at  $600 \text{ }^\circ\text{C}$  and  $900 \text{ }^\circ\text{C}$  HTA under an  $\text{O}_2$  environment [7]. Complex phase modifications between Fe oxides and silicates can be expected, including formation of magnetic FeO, which has active IR absorption bands [1,2]. The orientation-resolved optical technique proposed in this study is applicable to the analysis of orientation in femtosecond laser-induced nano-crystallisation inside multi-layered nano-stacks [8].

Olivine weathers quickly on the Earth's surface and has been found to be a promising candidate for accelerated weathering to sequester  $\text{CO}_2$  from the Earth's oceans and atmosphere to help combat climate change [9]. Olivine can absorb its own mass of  $\text{CO}_2$  when finely powdered. The European climate initiative Climate-KIC estimates that olivine could capture 850,000 tonnes of  $\text{CO}_2$ , and it has been used in small-scale projects, including as fertilizer and as a replacement for sand and gravel in landscaping projects [10]. According to the Goldich dissolution series, olivine is not stable and transforms into iddingsite in the presence of water [11]. Finding iddingsite on Mars would help determine if liquid water once existed on that planet [12]. Olivine is also relevant for detection of developing solar systems in Earth's neighbourhood since chondrites contain pallasites, which are a mix of iron–nickel and olivine. Furthermore, type-A asteroids have a surface that is dominated by olivine and are uncommon in our solar system but may be abundant in other planetary systems and could be detected by olivine spectral signatures once they have been determined under different conditions [13].

Here, we took advantage of the recently introduced four-polarisation cameras with wire grid polarisers integrated directly onto the pixels of a CMOS sensor. This allows for simultaneous detection of intensity at four orientations and access to the anisotropy of retardance and absorbance mapping; i.e., the absolute value and its azimuth (orientation). In the case of absorption-dominated transmission changes, it is shown that a cos-fit can be used for each pixel of the camera and obtained using only three points (three from four polarisation images). This technique is demonstrated for transmission and reflection modes using natural olivine micro-crystals, but it is fully transferable to other polarisation-resolved imaging techniques; e.g., bio-medical techniques [14,15], 3D optical coherent tomography [16,17], analysis of structural colours in natural materials [18], and industrial applications, such as edge detection of fast moving materials and workpieces [19].

## 2. Method and Samples

We used a 2<sup>12</sup>-level greyscale CMOS camera (CS505MUP1 Thorlabs) for imaging in the visible spectral range. The camera was set up with a Nikon OptoPhot-pol microscope for polarisation-resolved measurements and imaging. It is worth noting that a circular polariser, usually set just in front of a CCD or CMOS camera to homogenise the image, must be removed for imaging with the four-polarisation camera.

### 2.1. Method: Detection of Anisotropy

The linear dichroism or azimuthal dependence of the absorption of linearly polarised light is usually measured by changing the orientation of the incident polarisation and measuring (or imaging) the transmitted signal. For an absorber oriented at the angle  $\theta_{abs}$ , the absorbance  $A = -\log_{10} T$  is defined as follows [20]:

$$A(\theta) = \frac{A_{max} - A_{min}}{2} \cos(2\theta - 2\theta_{abs}) + \frac{A_{max} + A_{min}}{2}. \tag{1}$$

Here we adopted such a technique, but the measurement was carried out with non-polarised or circularly polarised incident light and took place at four selected polarisations with a four-polarisation camera. In the case of circular polarisation, we assumed that no circular dichroism existed within the sample. With the four-polarisation camera, four images are directly acquired in a single acquisition, while the incident light is non-polarised (isotropic random). This is a fast (instantaneous) imaging technique that is useful for monitoring and imaging of fast-changing events in real time; e.g., phase transitions induced by laser heating or applied pressure in diamond anvil cells.

By setting the circular polarisation at the IN-port (RHC or LHC) and without the  $\lambda/4$  waveplate before the four-polarisation camera, it is possible to measure the absorbance  $A$  of an image using Equation (1).

With linear polarisation illuminated onto the sample, the setup to measure birefringence and absorbance anisotropies was realised [21] (Figure 1a); i.e., a typical polariser-analyser arrangement only using a four-polarisation camera. Since absorbance is  $\pi$ -folded (same absorbance at 0 and  $\pi$ ) while birefringence has a twice higher angular frequency, the fit function to account for the two contributions in transmittance can be conveniently chosen as follows:

$$T(\theta) = [a_{\kappa} \cos^2(\theta - b_{\kappa}) + o_{\kappa}] + [a_n \cos^2 2(\theta - b_n) + o_n] \equiv Abs + Ret, \tag{2}$$

where  $a_{\kappa}$  and  $a_n$  are the amplitudes related to the absorbance  $Abs$  and retardance  $Ret$  contributions,  $b_{\kappa}$  and  $b_n$  are the orientation-dependent angles (which can be different for the two anisotropies), and  $o_{\kappa}$  and  $o_n$  are their corresponding offsets. Using  $\cos 2\theta = 2 \cos^2 \theta - 1$ , a normalised-form expression of Equation (2) for the absorbance part becomes  $T_{norm}(\theta) = \frac{1}{2} \cos(2\theta - 2\theta_{abs}) + \left[ \frac{1}{2} + \frac{o_{\kappa}}{a_{\kappa}} \right]$ . The last term defines the  $\theta$  angle-averaged transmittance  $T_{av}$  and the corresponding absorbance is  $A_{av} = -\log_{10} T_{av}$ . The ab-

sorption coefficient is found from the optical density  $A = 10^{-OD} \equiv e^{-\alpha d}$  as  $\alpha d = \ln 10OD \approx 2.3OD$ , where  $d$  is the thickness of the sample.

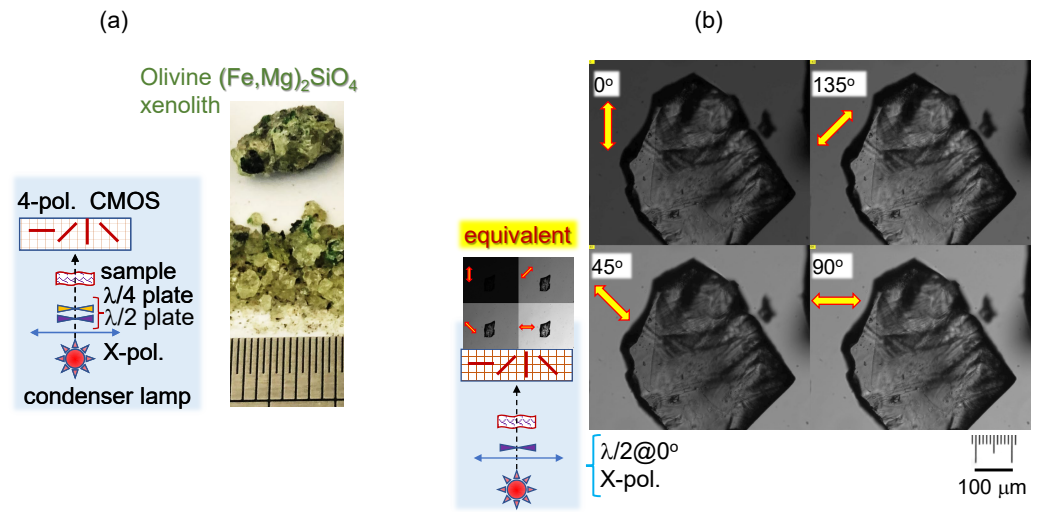


**Figure 1.** (a) Transmission setup with four-polarisation camera for measurements of absorbance and transmittance for characterisation of micro-grains of olivine. (b) Optical images of transmitted light at four polarisations. Measurements were carried out with linearly polarised illumination and four-polarisation detection (the achromatic  $\lambda/2$  plate was aligned with the linear polariser and used as a sample holder). This setup can be used for retardance and absorbance measurements. The circular polariser was realised using a pair of  $\lambda/2$  and  $\lambda/4$  plates at a  $\pm\pi/4$  angle for orientation of the  $\lambda/2$  plate (plastic pair, Edmund optics).

2.2. Mueller Matrices Used for Modelling of Transmittance

The Mueller matrix formalism was used to test the transmittance of the  $\lambda/4$  plate using the four-polarisation camera. The polariser at an angle of  $\varphi$  is given by the Mueller matrix  $M_{pol}$  [22]:

$$M_{pol}(\varphi) = \frac{1}{2} \begin{pmatrix} 1 & \cos 2\varphi & \sin 2\varphi & 0 \\ \cos 2\varphi & \cos^2 2\varphi & \cos 2\varphi \sin 2\varphi & 0 \\ \sin 2\varphi & \cos 2\varphi \sin 2\varphi & \sin^2 2\varphi & 0 \\ 0 & 0 & 0 & 0 \end{pmatrix}. \tag{3}$$

The matrix corresponds to the wire grid polariser on the pixels of the CMOS detectors with four polarisations. The angles  $\varphi$  were set at each quadrant of the camera to  $\varphi = 0, \pi/4, \pi/2,$  and  $3\pi/4$ , respectively. The retarder (e.g., a  $\lambda/4$  plate or the sample) with a phase retardance of  $\delta$  and retardance azimuth of  $\theta$  is given by the following:

$$M_{ret}(\theta, \delta) = \begin{pmatrix} 1 & 0 & 0 & 0 \\ 0 & \cos^2 2\theta + \cos \delta \sin^2 2\theta & (1 - \cos \delta) \sin 2\theta \cos 2\theta & \sin \delta \sin 2\theta \\ 0 & (1 - \cos \delta) \sin 2\theta \cos 2\theta & \sin^2 2\theta + \cos \delta \cos^2 2\theta & -\sin \delta \cos 2\theta \\ 0 & -\sin \delta \sin 2\theta & \sin \delta \cos 2\theta & \cos \delta \end{pmatrix}. \tag{4}$$

A quarter-wave plate with  $\delta_0 \equiv \pi/2$  phase retardance was added. The quarter-wave plate aligned along the  $\pi/4$  direction is given by (following from Equation (4)):

$$M_{\lambda/4}(\pi/4, \delta_0) = \begin{pmatrix} 1 & 0 & 0 & 0 \\ 0 & \cos \delta_0 & 0 & \sin \delta_0 \\ 0 & 0 & 1 & 0 \\ 0 & -\sin \delta_0 & 0 & \cos \delta_0 \end{pmatrix}. \tag{5}$$

The incident light was set to the horizontal (x-direction) so that it could be described by the Stokes vector  $\mathbf{S}_{IN} = (1, 1, 0, 0) \equiv (S_0, S_1, S_2, S_3)$ . Finally, the output light (Stokes vector) detected by the CMOS four-polarisation camera was indicated by the solution of the following matrix equation (the sample is represented by  $\mathbf{M}_{ret}(\theta, \delta)$ ):

$$\mathbf{S}_{OUT}(\varphi, \theta, \delta) = \mathbf{M}_{pol}(\varphi) \cdot \mathbf{M}_{ret}(\theta, \delta) \cdot \mathbf{M}_{\lambda/4}(\pi/4, \delta_0) \cdot \mathbf{S}_{IN}. \quad (6)$$

The last two terms in Equation (6) for the linear-horizontal incident polarisation (x-polarisation) in relation to the  $\lambda/4$  plate at  $\pm\pi/4$  angles define the Stokes vector of the light incident to the sample:

$$S^{inc} = \mathbf{M}_{\lambda/4}(\pm\pi/4) \cdot S_x = \begin{pmatrix} 1 & 0 & 0 & 0 \\ 0 & 0 & 0 & \pm 1 \\ 0 & 0 & 1 & 0 \\ 0 & \mp 1 & 0 & 0 \end{pmatrix} \cdot \begin{pmatrix} 1 \\ 1 \\ 0 \\ 0 \end{pmatrix} = \begin{pmatrix} 1 \\ 0 \\ 0 \\ \mp 1 \end{pmatrix}. \quad (7)$$

With this simplification and use of the sample's (retarder's) expression  $\mathbf{M}_{ret}(\theta, \delta)$  with the four-polarisation analyser angles  $\varphi \equiv (0, \pi/4, \pi/2, -\pi/4)$  in the polariser matrix  $\mathbf{M}_{pol}(\varphi)$ , one obtains the output intensity at the four-polarisation camera (the Stokes  $S_0$  parameter measured experimentally).

### 2.3. Annealed Olivine Samples

The samples in this study were volcanic olivine xenoliths (Mortlake, Victoria, Australia; Figure 1a). Sub-millimetre grains of olivine were subjected to high-temperature annealing (HTA) at 1200–1500 °C for 1–2 h. Such HTA treatment made the samples magnetised in the presence of O<sub>2</sub> flow.

The HTA was carried out using a Nabertherm tube furnace; see the discussion and optical characterisation in Section 3.3 for samples annealed at 1500 °C for 2 h in O<sub>2</sub> flow. Magnetisation of the samples was evident from their strong attraction to Nb or Sm magnets. The O<sub>2</sub> flow was required to magnetise the initial weakly magnetic olivine xenolith samples ((Fe, Mg)<sub>2</sub>SiO<sub>4</sub> xenoliths from Mortlake, Victoria, Australia); only the smallest micro-grains were attracted to the Nd magnet in the case of the pristine olivine, while large samples with sub-centimetre cross-sections were attracted to the same magnet after HTA. The origin of the magnetisation is under investigation, and it is out of the scope of this study focused on optical polariscopy. Several temperatures were tested for HTA in the range of 600–1200 °C (600, 800, 1000, 1200 °C) in O<sub>2</sub> flow. However, samples were not magnetised even when they changed colour above 900 °C, possibly due to hematite  $\alpha$ -Fe<sub>2</sub>O<sub>3</sub> formation [23]. Even after HTA at the highest temperature of 1500 °C, samples maintained their grainy structure without turning into glassy substances solidified from a molten phase. For optical polariscopy, the annealed olivine xenolith was hammer-smashed into micro/macro-particles, aiming at obtaining samples tens of micrometers in size, and they could also be partly transparent. Those micro-particles were magnetised, as revealed by their ordering on a slide glass (1 mm thick), using Sm-Co and Nd magnets (Section 3.3).

## 3. Results and Discussion

### 3.1. Four-Polarisation Detection of Transmitted Intensity

Figure 1a shows the setup for the realisation of the polariser–analyser and one analyser measurement in the transmission mode for linear or circular polarisation incident to the sample. Such a setup can be rendered sensitive to both retardance and absorbance (b) and only absorbance when the equivalent of two or one polarisers is utilised. Notably, the setup with circularly polarised light (isotropic in terms of the polarisation incident to the sample) can be used to measure linear dichroism if there is no circular dichroism in the sample; i.e., the polarisation-isotropic incident light is prepared by a linear polariser and achromatic  $\lambda/4$  waveplate at  $\pm\pi/4$  orientation (Figure 2). Employing the four-polarisation camera using an achromatic  $\lambda/2$  plate aligned with linearly polarised incident light resulted in

four different images (Figure 1b); a plastic polariser was used as a sample holder. For some mutual orientations of the sample and waveplate, one of the four images had low intensity (cross-polarised; see inset in Figure 1b). As shown later, even three images acquired at three orientations were enough for the best fit and the extraction of the orientation azimuth of the absorbers.

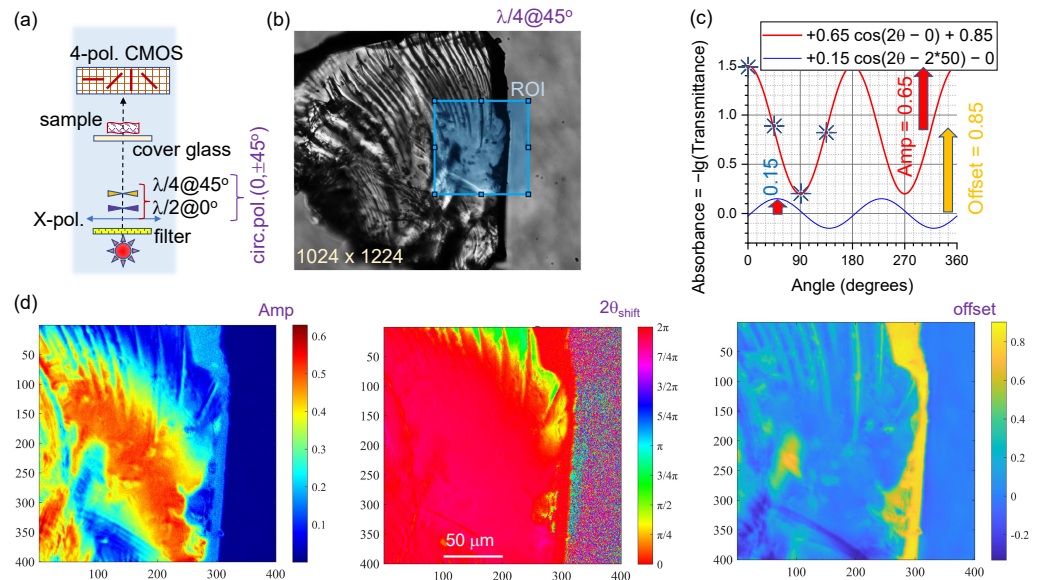


**Figure 2.** Absorbance measurements for an olivine micro-particle. (a) Absorbance measurement with linearly polarised illumination and four-polarisation detection. A pair of  $\lambda/2$  and  $\lambda/4$  plates were used to make an achromatic plastic circular polariser (Edmund optics) at  $0^\circ$  orientation; this corresponds to the linearly polarised illumination (the x-polarisation of the microscope condenser). (b) Optical image of olivine micro-grain using combined intensity with the four-polarisation camera. Illumination was set as circular using a single  $\lambda/4$  plastic plate (Edmund optics) at  $45^\circ$  orientation and a 550 nm bandpass filter ( $\sim 20$  nm). (c) Absorbance  $A \equiv -\log_{10} T$  spectra for two distinct experimental results selected from (d) to illustrate the fit. The amplitude  $Amp$  and offset  $Offset$  values were retrieved from the best fit. Four markers at the four-polarisation camera orientations are shown. (d) The fit results for each pixel for the values of  $Amp$ ,  $Offset$ , and  $2\theta_{shift}$  over a selected region of interest (ROI). The orientation  $2\theta_{shift}$  corresponds to the largest absorbance.

Equation (1) was applied for the absorbance plot at each pixel under circularly polarised illumination for the olivine micro-particle (Figure 3). A  $\lambda/4$  waveplate was used to set circularly polarised light, along with a 550 nm filter with  $\sim 20$  nm bandwidth. The best fit was obtained for amplitude  $Amp = (A_{max} - A_{min})/2$ , the azimuth of the absorber angle  $2\theta_{abs} = 2\theta_{shift}$ , and offset  $offset = (A_{max} + A_{min})/2$  for a single pixel using Matlab. In the fit, there were regions with negative offset, which corresponded to a phase change (sin to cos). The strong absorbance near the edges (low  $Amp$  and high  $Offset$ ) was due to the light-scattering contribution, since the collection of light corresponded to the angle defined by the numerical aperture  $NA = 0.45$  of the  $20\times$  objective lens (Nikon). The resolution, defined as the radius of the Airy disk of a plane wave focusing, was  $r = 0.61\lambda/NA \approx 0.72 \mu\text{m}$  at the green  $\lambda = 530$  nm wavelength.

The described four-polarisation imaging with a four-point absorbance fit (Equation (2)) under isotropic incident polarisation (circular or random) provided a map of average optical density  $OffsetA(x, y)$ , its amplitude  $Amp(x, y)$ , and the azimuthal orientation of the absorbers  $\theta_{shift}$  at the pixel level. The quality of the fit was judged from the standard

deviation map  $\sigma(x, y) = \sqrt{[\sum_i (I_{\theta(i)}^{exp}(x, y) - I_{\theta(i)}^{fit}(x, y))^2]/4}$ . Figure 3 shows the results. For the high-fidelity fit, there was no difference in  $\sigma$  at the regions with and without micro-grains (Figure 3c) with  $\sigma < 10^{-5}$  (the maximum-intensity offset and amplitude values were

~2000). The same procedure can be carried out at different wavelengths. With illumination of the sample with isotropic polarisation, all four images in the four-polarisation camera had intensity values that were satisfactory for the fit at the four values of  $\theta_i$ . However, for the case with linearly polarised illumination, one segment of the four-polarisation-camera fit usually had overly small values for the intensity (see the dark segment in the inset of Figure 1b), and calculation of the absorbance (a ratio) resulted in an unreliable fit. In such cases, only three  $\theta_i$  values could be used to extract the three parameters  $Amp$ ,  $2\theta_{shift}$ , and  $Offset$ , as described next.

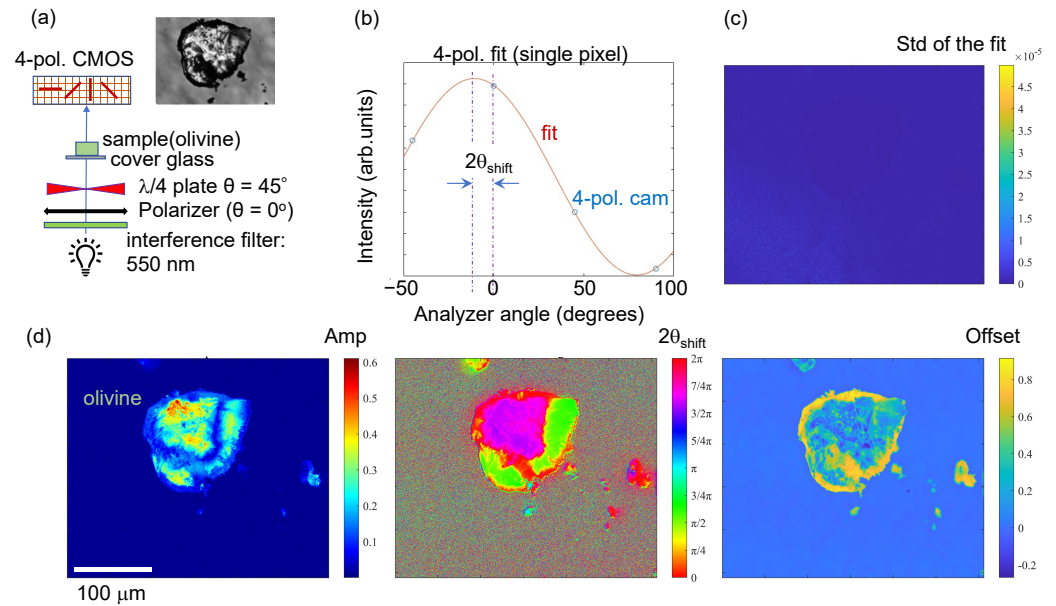


**Figure 3.** (a) Setup for sample's illumination with circular-polarisation (isotropic) illumination and four-polarisation camera imaging. (b) Four-point fit of absorbance  $A = -\lg(T(\theta)) \equiv -\lg[I_T(\theta)/I_0(\theta)] = Amp \times \cos(2\theta - 2\theta_{shift}) + Offset$ . (c) The standard deviation  $\sigma$  of the intensity fit  $I(\theta)$ :  $\sigma = \sqrt{[\sum_i (I^{exp}(\theta_i) - I^{fit}(\theta_i))^2]/4}$ , with  $i$  being the index for four-polarisation angles. (d) Maps for the best-fit parameters amplitude  $Amp$ , phase azimuth  $\theta_{shift}$  and  $Offset$  are shown in corresponding panels for the circularly polarised illumination. The offset had no bounds defined for the fit and the angle  $2\theta_{shift}$  was bound to the  $0 - 2\pi$  range during the fitting procedure.

### 3.2. Three-Point Fit of Four-Polarisation Camera Images

When the two-polariser system was used with the IN- and OUT-ports (a cross-Nicol) sensitive to retardance and absorbance changes, there was a large difference in the intensity of the four-polarisation camera segments (Figure 1b). The best fit for the transmitted intensity  $I_T$  was obtained with a generic expression  $I_T = Amp \times \cos(2\theta - 2\theta_{shift}) + Offset$  and is shown in Figure 4 for linearly polarised illumination with two different orientations of a  $\lambda/2$  plate. The absorption azimuth  $2\theta_{shift}$  was close to  $0^\circ$  or  $180^\circ$ , which, for a randomly chosen micro-grain, implies the absence of a preferential orientation. This is understandable since olivine is transparent in the visible spectral range (see the central inset in Figure 1). Importantly, the use of four intensity images for the calculation of the transmittance  $T(\theta) \equiv I_T(\theta)/I_0(\theta)$  using the acquired images was not successful due to very low intensity in one of the quadrant images; we even checked that it did not have a division by zero error. However, for the fit with a harmonic cos function with three parameters, only three points were enough and allowed for the extraction of single-pixel transmittance  $T = I_T/I_0$  and, hence, absorbance  $A = -\log_{10} T$ . The obtained maps from three-angle fit are shown in Figure 4. This procedure relied on the three highest-intensity points measured (from the four points of the four-polarisation camera).

The three-point best fit with  $T = Amp \times \cos(2\theta - 2\theta_{shift}) + Offset$  was also carried out for a linear incident polarisation using a  $\lambda/4$  plate at 0 degrees (Figure 5). In this fit, the condition requiring only positive values for  $Amp > 0$  was enforced and also  $0 < 2\theta_{shift} < 2\pi$ , as expected for the absorption-dominated azimuthal transmission. The three-point fit closely matched the calculated absorbance given by Equation (1) (Figure 2d) for the circularly polarised (isotropic polarisation) case. The three-point fit at the highest intensity values with the four-polarisation camera images was validated for  $\lambda/4$  and  $\lambda/2$  plates.

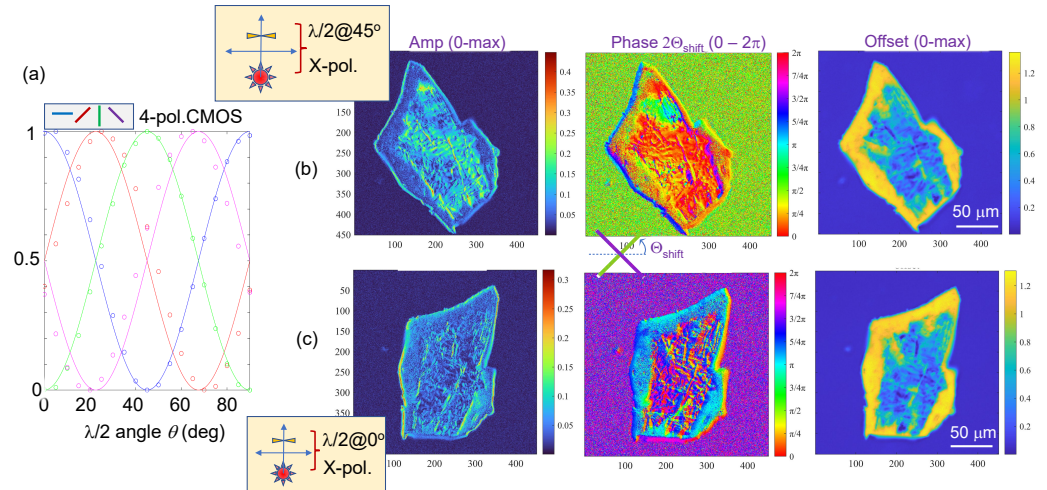


**Figure 4.** (a) Transmittance of the  $\lambda/2$  plate at different orientation angles: dots—experiment, lines—Mueller matrix calculations (see Section 2.2); the selected area of  $1224 \times 1024$  pixels was averaged for plotting. Three-point fit to  $T(\theta) \equiv I_T(\theta)/I_0(\theta) = Amp \times \cos(2\theta - 2\theta_{shift}) + Offset$ . Maps for the best-fit parameters amplitude  $Amp$ , phase azimuth  $\theta_{shift}$ , and  $Offset$  are shown in corresponding panels for the linearly polarised illumination with different orientations of the  $\lambda/2$  plate:  $+\pi/4$  (a) and 0 (b). Amplitude and offset were set to be positive and the angle  $2\theta_{shift}$  was bound to the  $0 - 2\pi$  range during the fitting procedure. An achromatic polymer  $\lambda/2$  waveplate was used as a sample holder. A cross with the  $\theta_{shift}$  marker between phase maps in (b,c) illustrates the  $\perp$  orientation of the background colour maps, as expected for the  $\pi/2$  phase difference for the  $\lambda/4$  plate at 0 vs.  $\pi/4$  orientations.

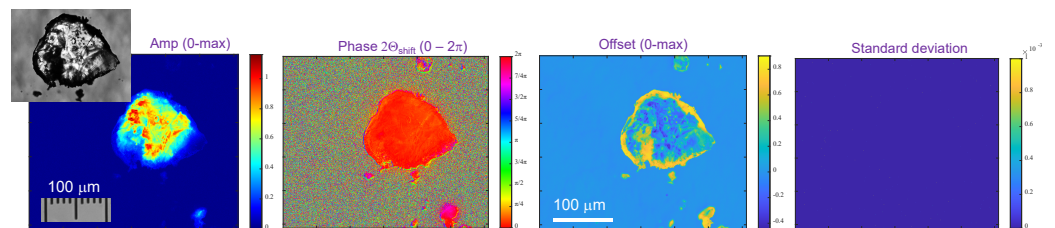


**Figure 5.** Three-point ( $0, \pm\pi/4$ ) fit of absorbance for the illumination of olivine grains by linear polarised light using  $\lambda/4$  plate at  $0^\circ$  (same sample as in Figure 3). The standard deviation  $\sigma < 10^{-3}$  showed a good fit for the three points (angles). An interference bandpass filter with  $550 \pm 10$  nm was used for illumination.

### 3.3. Annealed Olivine under Reflection (Three-Point) Polariscopy

The samples of olivine xenolith were annealed at  $1500^\circ\text{C}$  temperature for 2 h in  $\text{O}_2$  flow. This made them magnetic, as shown in Figure 6a, before mechanical fragmentation. After fragmentation, magnetic particles/grains were assembled using an Nd magnet (NdFeB; washer-type) placed on a Sm-Co magnet (disk-type). Since olivine subjected to HTA did not turn optically transparent and had a black-brown appearance, reflection-type

microscopy was used for polarisation analysis with a four-polarisation camera (Figure 6b). Two achromatic  $\lambda/4$  waveplates were used at the IN- and OUT-ports with the sample placed on an Al foil (or Au mirror) serving as a back-reflecting mirror. The  $\lambda/4$  waveplates were crossed by the orientation of their slow axis, hence compensating the phases  $\pm\pi/2$  of each other. They were used for qualitative inspection if optical activity or circular dichroism existed in the semi-transparent parts of the high-temperature-annealed olivine. For reflection microscopy under linear polarisation, the orientation of the  $\lambda/2$  or  $\lambda/4$  waveplates was set at  $0^\circ$  (slow axis aligned with linear polariser at the IN-port). In such cases, no  $\lambda/4$  waveplate was used before the four-polarisation detector (OUT-port).

Figure 7 shows optical images of high-temperature-annealed olivine in  $O_2$  with clearly visible micro-crystallites in a dark rock. When  $N_2$  flow was used, there was almost no colouration change. This sample was fractionated to produce a small grain smaller than 1 mm in size. The grain was captured with a Nd magnet (washer) to confirm its magnetisation and brought into the optical path for reflectance measurements. The same three-point fitting procedure as shown for transmittance was applied for reflectance. Figure 8 shows the fitting results. Micro-crystallites in a larger ( $\sim 1$  mm) sample of olivine were recognised by their edges (top row in Figure 8). For illumination by circularly polarised light, a  $\lambda/4$  plate was used and a smaller grain was set with a Au mirror (Figure 8). The colour of the phase map showed a  $\pi/2$  change in the background between the 0 and  $\pm\pi/4$  orientations of the  $\lambda/4$  plate. As we showed earlier, the structure patterns could be recognised in reflection/scattering-mode imaging with the same camera, even when optical resolution was poor for the small feature size [24]. For quantitative measurement of reflectance  $R$ , gold-coated ( $\sim 60$  nm) cover glass was used as a reference (or as a sample holder). A simpler setup for RHC and LHC polarisations can be employed using plastic polariser films (CIR RH or LH, Edmund optics), which are combined polariser and  $\lambda/4$  pairs.

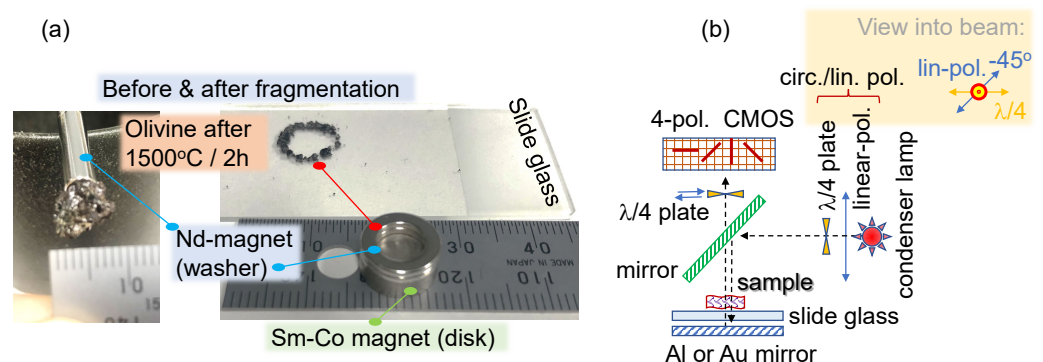


**Figure 6.** High-temperature annealing (HTA) of olivine xenolith. (a) Sample annealed at  $1500^\circ\text{C}$  for 2 h held on a magnet rod (left) and after its fragmentation (right). Micro/millimetre-sized grains of high-temperature-annealed olivine were gathered by magnets placed below the slide glass for microscopy observation. (b) A reflection-type microscope assembly was used for this study (set up with Nikon Optiphot-pol). Two plastic achromatic  $\lambda/4$  waveplates were used to provide the capability to detect circular dichroism or optical activity. The slow axes of the plates were crossed and the linear polariser was rotated  $\pm\pi/4$  to set up the right or left circular polarisations (RCP/LCP), respectively. The convention of the sign was  $-\pi/4$  for the anti-clockwise rotation of the linear polariser at the IN-port (see inset in (b)).

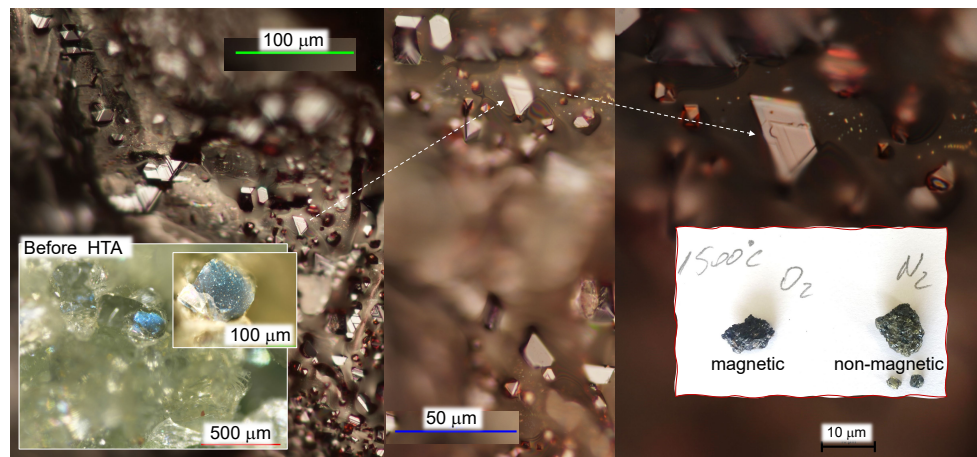


**Figure 7.** High-temperature annealing (HTA) of olivine xenolith. Optical images at increasing magnification (left to right) of a sample annealed at 1500 °C for 2 h in O<sub>2</sub> flow. The left inset shows typical olivine macro-grains before annealing. The right inset shows a photo of samples after HTA at 1500 °C for 2 h in O<sub>2</sub> and N<sub>2</sub> flow.

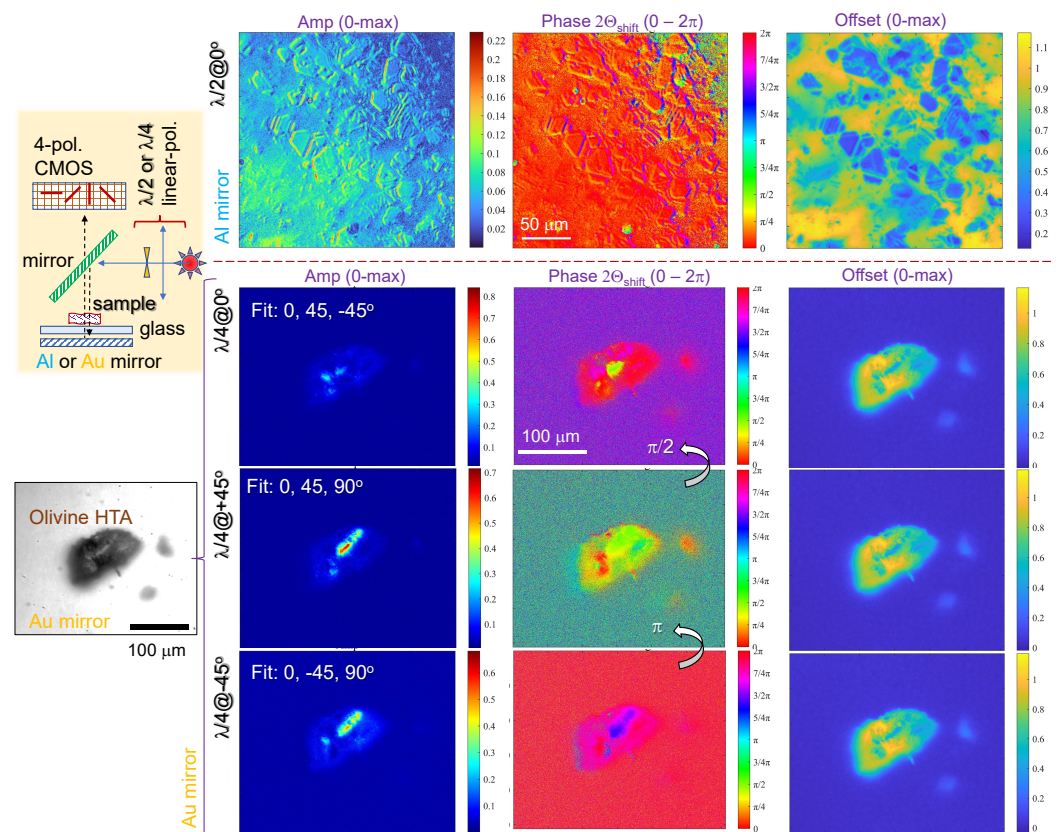


**Figure 8.** High-temperature-annealed olivine (magnetic). Reflectance spectra were fit with the three points that were most intense in the four-polarisation camera; reflection from the macro-particle (~1 mm in size; top row) with linearly polarised illumination ( $\lambda/2$  at  $0^\circ$ ). Smaller grains of high-temperature-annealed olivine: linear and circular polarised illumination ( $\lambda/4$  at  $0$  (lin.) and  $\pm 45^\circ$  (circ.)); the left inset shows schematics of the reflection experiment. HTA took place at 1500 °C for 2 h in O<sub>2</sub>. The grain was fixed to a washer magnet and brought into reflection mode (top row). The three-point-fit method was used for the reflectance  $R = Amp \times \cos(2\theta - 2\theta_{shift}) + Offset$ ; the background was measured from a Au mirror with the sample moved out of the beam. Standard deviation maps (not shown) indicated  $\sigma < 10^{-3}$  for all measurements.

#### 4. Conclusions and Outlook

This study introduced polarisation analysis at the visible spectral range for 3D complex samples that are usually further scrutinised at the IR and THz spectral range with correspondingly reduced resolutions: visible  $\sim 1 \mu\text{m}$ , IR  $\sim 10 \mu\text{m}$ , THz  $\sim 100 \mu\text{m}$ . By using polarisation analysis at the visible spectral range with a four-polarisation camera, simple four- or three-point (angles) fitting of transmitted or reflected light provided detailed maps of the sample's structure related to its shape, composition, and thickness. When tracing changes during various thermal treatments (e.g., HTA) with gas-sample reactions (olivine with  $\text{CO}_2$ ), polarisation-resolved optical imaging can provide useful pinpoint definitions of the locations of the induced changes, the precipitation of new phases, changes related to melting and surface tension-induced flows.

The three-point fit of the four-polarisation camera images was introduced and validated for transmittance and reflectance. As a prototype material, olivine in its original and thermally modified magnetic states was optically mapped using polarisation imaging. The proposed analysis is applicable to linearly and circularly polarised light. Reflectivity change in materials due to dielectric-to-metallic state change or formation of micro-precipitates could be visualised using polarisation analysis with two perpendicular polarisations [25]. The polarisation-resolved imaging presented here can be used for analysis of 3D polymerised structures where hatching of the 3D volume and pulse-to-pulse overlap along a linear scan are important for the structural quality of the 3D polymerised object [26]. Laser-ablated targets in liquids form chains of magnetised nanoparticles [27,28] whose orientation can be recognised even below the spatial resolution using the proposed polarisation analysis [5].

**Author Contributions:** Conceptualization, J.M., M.R. and S.J.; methodology, M.R., D.S., S.K. and J.V.; software development, S.K. and M.R.; validation, S.H.N., H.-H.H., P.M., D.M. and D.S.; formal analysis, S.K., D.S., M.R. and J.M.; investigation, T.K., P.M., H.-H.H., D.M. and J.V.; resources, J.M.; data curation, S.K., D.S. and M.R.; writing—original draft preparation, S.K. and S.J.; writing—review and editing, all the authors; visualization, S.K. and S.J.; supervision, J.M. All authors have read and agreed to the published version of the manuscript.

**Funding:** This research was funded by the ARC Linkage LP190100505 project. J.M. and M.R. were funded by JSPS KAKENHI grant no. 22H02137 and JST CREST grant no. JPMJCR19I3. M.R. was funded by JSPS KAKENHI grant no. 22K14200. The polarisation analysis at visible wavelengths reported in this study is part of the recent synchrotron-FTIR beamtime experiment performed on the Infrared Microspectroscopy (IRM) beamline at the Australian Synchrotron (Proposal ID. M18753).

**Data Availability Statement:** Data can be made available upon reasonable request.

**Acknowledgments:** We are grateful to a volunteer fossicking guide Joe Mooney from Mortlake, Victoria, for leading our collection of olivine xenoliths from Mortlake quarry in 2016.

**Conflicts of Interest:** The authors declare no conflict of interest.

#### References

1. Schrettle, F.; Kant, C.; Lunkenheimer, P.; Mayr, F.; Deisenhofer, J.; Loidl, A. Wüstite: Electric, thermodynamic and optical properties of FeO. *Eur. Phys. J. B* **2012**, *85*, 164. [CrossRef]
2. Koike, C.; Matsuno, J.; Chihara, H. Variations in the Infrared Spectra of Wüstite with Defects and Disorder. *Astrophys. J.* **2017**, *845*, 115. [CrossRef]
3. Scarcelli, G.; Yun, S.H. Confocal Brillouin microscopy for three-dimensional mechanical imaging. *Nat. Photonics* **2008**, *2*, 39. [CrossRef]
4. Traverso, A.J.; Thompson, J.V.; Steelman, Z.A.; Meng, Z.; Scully, M.O.; Yakovlev, V.V. Dual Raman-Brillouin Microscope for Chemical and Mechanical Characterization and Imaging. *Anal. Chem.* **2015**, *87*, 7519–7523. [CrossRef]
5. Honda, R.; Ryu, M.; Moritake, M.; Balcytis, A.; Mizeikis, V.; Vongsvivut, J.; Tobin, M.J.; Appadoo, D.; Li, J.L.; Ng, S.H.; et al. Infrared Polariscopy Imaging of Linear Polymeric Patterns with a Focal Plane Array. *Nanomaterials* **2019**, *9*, 732. [CrossRef]
6. Ryu, M.; Nishijima, Y.; To, S.M.N.; Hashizume, T.; Matsubara, R.; Kubono, A.; Hu, J.; Ng, S.; Juodkazis, S.; Morikawa, J. Hyperspectral Molecular Orientation Mapping in Metamaterials. *Appl. Sci.* **2021**, *11*, 1544. [CrossRef]
7. Kadziolka-Gawel, M.; Adamczyk, Z.; Kalinowski, L. Mössbauer study of changes in Olivine after heating in air. *Can. Mineral.* **2019**, *57*, 105–115. [CrossRef]

8. Ricca, R.; Bellouard, Y. Single-Layer Subwavelength Femtosecond-Laser-Induced Confined Nanocrystallization in Multistack Dielectrics. *Phys. Rev. Appl.* **2023**, *19*, 044035. [CrossRef]
9. Schuiling, R.D. Olivine against Climate Change and Ocean Acidification. 2011. Available online: <http://www.innovationconcepts.eu/res/literatuurSchuiling/olivineagainstclimatechange23.pdf> (accessed on 10 September 2023).
10. van Dongen, T. One Tonne of Olivine Sand Can Take in up to One Tonne of CO<sub>2</sub>. 2021. Available online: <https://www.dezeen.com/2021/06/15/carbon-capture-material-library-aireal-olivine-teresa-van-dongen/> (accessed on 10 September 2023).
11. Kuebler, K.; Wang, A.; Haskin, L.; Jolliff, B. A Study of Olivine Alteration to Iddingsite Using Raman Spectroscopy. *Astrophys. J.* **2006**, *34*, 1953.
12. Swindle, T.; Treiman, A.; Lindstrom, D.; Burkland, M.; Cohen, B.; Grier, J.; Li, B.; Olson, E. Noble gases in iddingsite from the Lafayette meteorite: Evidence for liquid water on Mars in the last few hundred million years. *Meteorit. Planet. Sci.* **2000**, *35*, 107–115. [CrossRef]
13. Vernazza, P.; Ferrais, M.; Jorda, L.; Hanus, J.; Carry, B.; Marsset, M.; Broz, M.; Fetick, R.; Viikinkoski, M.; Marchis, F.; et al. VLT/SPHERE imaging survey of the largest main-belt asteroids: Final results and synthesis. *Astron. Astrophys.* **2021**, *654*, A56. [CrossRef]
14. Gassner, C.; Vongsvivut, J.; Ng, S.; Ryu, M.; Tobin, M.; Juodkazis, S.; Morikawa, J.; Wood, B. Linearly Polarized Infrared Spectroscopy for the Analysis of Biological Materials. *Appl. Spectrosc.* **2023**, *in press*. [CrossRef]
15. He, C.; He, H.; Chang, J.; Chen, B.; Ma, H.; Booth, M. Polarisation optics for biomedical and clinical applications: A review. *Light. Sci. Appl.* **2021**, *10*, 194. [CrossRef]
16. Roth, J.; Kozak, J.; Yazdanfar, S.; Rollins, A.; Izatt, J. Simplified method for polarization-sensitive optical coherence tomography. *Opt. Lett.* **2001**, *26*, 1069–1071. [CrossRef]
17. de Boer, J.; Hitzengerger, C.; Yasuno, Y. Polarization sensitive optical coherence tomography—A review. *Biomed. Opt. Express* **2017**, *8*, 1838–1873. [CrossRef]
18. Linklater, D.; Vailionis, A.; Ryu, M.; Kamegaki, S.; Morikawa, J.; Mu, H.; Smith, D.; Maasoumi, P.; Ford, R.; Katkus, T.; et al. Structure and Optical Anisotropy of Spider Scales and Silk: The Use of Chromaticity and Azimuth Colors to Optically Characterize Complex Biological Structures. *Nanomaterials* **2023**, *in press*. [CrossRef]
19. Onuma, T.; Otani, Y. A development of two-dimensional birefringence distribution measurement system with a sampling rate of 1.3 MHz. *Opt. Commun.* **2014**, *315*, 69–73. [CrossRef]
20. Hikima, Y.; Morikawa, J.; Hashimoto, T. FT-IR Image Processing Algorithms for In-Plane Orientation Function and Azimuth Angle of Uniaxially Drawn Polyethylene Composite Film. *Macromolecules* **2011**, *44*, 3950–3957. [CrossRef]
21. Honda, R.; Ryu, M.; Moritake, M.; Balcytis, A.; Mizeikis, V.; Vongsvivut, J.; Tobin, M.J.; Appadoo, D.; Li, J.L.; Ng, S.H.; et al. Hyperspectral mapping of anisotropy. *Nanoscale Horiz.* **2019**, *4*, 1443–1449.
22. Collett, E. *Polarization*, 3rd ed.; Field guides; SPIE Press: Bellingham, DC, USA, 2005.
23. Roberts, A.; Zhao, X.; Hu, P.; Abrajevitch, A.; Chen, Y.H.; Harrison, R.; Heslop, D.; Jiang, Z.; Li, J.; Liu, Q.; et al. Magnetic Domain State and Anisotropy in Hematite ( $\alpha$ -Fe<sub>2</sub>O<sub>3</sub>) From First-Order Reversal Curve Diagrams. *J. Geophys. Res. Solid Earth* **2021**, *126*, e2021JB023027. [CrossRef]
24. Ng, S.; Allan, B.; Ierodiaconou, D.; Anand, V.; Babanin, A.; Juodkazis, S. Drone Polariscopy—Towards Remote Sensing Applications. *Eng. Proc.* **2021**, *11*, 46.
25. Chen, H.; Wolff, L. Polarization Phase-Based Method For Material Classification In Computer Vision. *Int. J. Comput. Vis.* **1998**, *28*, 73–83. [CrossRef]
26. Fritzsche, S.; Pauw, B.; Weimann, C.; Sturm, H. First of its kind: A test artifact for direct laser writing. *Meas. Sci. Technol.* **2023**, *34*, 075004. [CrossRef]
27. Semaltianos, N.; Karczewski, G. Laser Synthesis of Magnetic Nanoparticles in Liquids and Application in the Fabrication of Polymer–Nanoparticle Composites. *ACS Appl. Nano Mater.* **2021**, *4*, 6407–6440. [CrossRef]
28. Jakobi, J.; Petersen, S.; Menéndez-Manjón, A.; Wagener, P.; Barcikowski, S. Magnetic Alloy Nanoparticles from Laser Ablation in Cyclopentanone and Their Embedding into a Photoresist. *Langmuir* **2010**, *26*, 6892–6897. [CrossRef]

**Disclaimer/Publisher’s Note:** The statements, opinions and data contained in all publications are solely those of the individual author(s) and contributor(s) and not of MDPI and/or the editor(s). MDPI and/or the editor(s) disclaim responsibility for any injury to people or property resulting from any ideas, methods, instructions or products referred to in the content.